Opposed hemodynamic responses following increased excitation and parvalbumin-based inhibition

Joonhyuk Lee[1], Chloe L Stile[1], Annie R Bice[1],
Zachary P Rosenthal[2], Ping Yan[2], Abraham Z Snyder[1],
Jin-Moo Lee[2,3] and Adam Q Bauer[1,3]

Abstract
Understanding cellular contributions to hemodynamic activity is essential for interpreting blood-based brain mapping signals. Optogenetic studies examining cell-specific influences on local hemodynamics have reported that excitatory activity results in cerebral perfusion and blood volume increase, while inhibitory activity contributes to both vasodilation and vasoconstriction. How specific subpopulations of interneurons regulate the brain's blood supply is less examined. Parvalbumin interneurons are the largest subpopulation of GABAergic neurons in the brain, critical for brain development, plasticity, and long-distance excitatory neurotransmission. Despite their essential role in brain function, the contribution of parvalbumin neurons to neurovascular coupling has been relatively unexamined. Using optical intrinsic signal imaging and laser speckle contrast imaging, we photostimulated awake and anesthetized transgenic mice expressing channelrhodopsin under a parvalbumin promoter. Increased parvalbumin activity reduced local oxygenation, cerebral blood volume, and cerebral blood flow. These "negative" hemodynamic responses were consistent within and across mice and reproducible across a broad range of photostimulus parameters. However, the sign and magnitude of the hemodynamic response resulting from increased parvalbumin activity depended on the type and level of anesthesia used. Opposed hemodynamic responses following increased excitation or parvalbumin-based inhibition suggest unique contributions from different cell populations to neurovascular coupling.

Introduction

Neurovascular coupling (NVC) is the process through which changes in local neural activity are coupled to changes in cerebral blood flow (CBF). Views on underlying mechanisms of NVC have gradually shifted from a feedback model, i.e. that metabolic by-products of brain activity primarily drive CBF changes, to also include a feedforward mechanism, where CBF delivery is driven by neurovascular signaling pathways.[1,2] An important link connecting neural activity and CBF regulation is the ability of certain cell populations to mediate the diameter of local blood vessels through vasoactive messengers.[3–5] Functional hyperemia induced by peripheral whisker stimulation (WS) increases activity in pyramidal cells releasing the prostanoid-synthesizing enzyme cyclooxygenase-2 causing an increase in CBF.[6,7] Somatosensory stimuli also activate γ-aminobutyric acid (GABA) interneurons.[7] Interneurons produce vasoactive neurotransmitters and neuromodulators and have close involvement

[1]Department of Radiology, Washington University School of Medicine, St. Louis, MO, USA
[2]Department of Neurology, Washington University School of Medicine, St. Louis, MO, USA
[3]Department of Biomedical Engineering, Washington University School of Medicine, St. Louis, MO, USA

Corresponding author:
Adam Q Bauer, Washington University School of Medicine, Scott McKinley Research Building, 4515 McKinley Ave, St. Louis, MO 63110, USA.
Email: aqbauer@wustl.edu

with cerebral microvessels,[4] positioning them as crucial mediators of NVC.[4,7] Indeed, changes in pyramidal cell activity, modulated by specific types of GABAergic interneurons, have been shown to drive stimulus-evoked responses in the rat barrel cortex.[7] In slice preparations, electrical stimulation of different subsets of GABAergic interneurons can cause either local vasodilation or vasoconstriction depending on which cell type is stimulated.[4,8]

More recent studies using optogenetics have shown that targeting the vesicular GABA transporter (VGAT) results in increased CBF despite suppression of local spontaneous neural activity.[9–11] These CBF increases persist when glutamatergic or GABAergic activity is pharmacologically blocked,[9] suggesting that VGAT-expressing neurons can regulate flow independently of their local neural network. In the same transgenic mouse line, Uhlirova et al.[10] reported that VGAT photostimulation (PS) results in a biphasic vascular response (dilation followed by constriction) and identified the vasoconstrictive mechanism as neuropeptide Y (NPY) acting on Y1 receptors. However, because all VGAT-expressing neurons were targeted, it was not determined if different subpopulations of GABAergic neurons can differentially regulate distinct phases of the vascular response. While an area of active study, how or if different types of interneurons can elicit opposite hemodynamic responses is currently unresolved.[12–14]

As the largest subpopulation (~40%) of GABAergic neurons,[15] parvalbumin (PV)-expressing interneurons are crucial to many brain processes, including neuroplasticity,[16] brain development,[17] and cortical gamma oscillation regulation.[18,19] The lack of properly functioning PV interneurons has been linked to numerous disorders including autism,[20] schizophrenia,[21] and post-traumatic stress disorder.[22] Despite this neuronal population's significance to normal brain function, the role of PV-interneurons in NVC has been less examined. PV-expressing inhibitory interneurons are not known to co-express any vasoactive compounds that produce constriction (e.g. NPY or somatostatin (SOM)) or dilation (e.g. vasoactive intestinal peptide (VIP) or nitric oxide synthase (NOS)).[4,10,23] However, evidence suggests that PV cells are able to affect local hemodynamic activity. In tissue slices, stimulation of PV neurons constricted local arterioles.[8] In vivo, increased PV activity in isoflurane anesthetized rats produced local positive BOLD responses during the stimulation period.[24] More recent reports have demonstrated increases in CBF following PV stimulation well after stimuli had been removed.[13,14] These different observations invite further investigation of how PV-expressing cells regulate the brain's blood supply.

In this study, we investigated the role of PV-positive cells in NVC under different photostimulus parameters and states of arousal. Our results demonstrate a critical role in PV-expressing interneurons in NVC by inhibiting local circuitry to reduce cerebral perfusion, oxygenation, and metabolic demand. These findings highly depended on the type and depth of anesthetic administered and motivated the use of awake imaging in studies focused on examining cell specific contributions to NVC.

Materials and methods

Ethics statement

All animal studies were approved by the Washington University School of Medicine Animal Studies Committee under guidelines and regulations consistent with the Guide for the Care and Use of Laboratory Animals, Public Health Service Policy on Humane Care and Use of Laboratory Animals, and the Animal Welfare Act and Animal Welfare Regulations. Animal reporting is according to ARRIVE guidelines.

Mouse breeding

Eight male mice expressing channelrhodopsin (ChR2) under a PV promoter (PV-ChR2) aged between five and eight months were used for experimentation. PV-ChR2 mice were generated using Cre-Lox recombination (parent strains: PV-Cre, B6.129P2-Pvalb$^{tm1(cre)Arbr}$/J, Stock number: 017320; Lox-ChR2, B6;129S-Gt(ROSA)26Sor$^{tm31(CAG-COP4*H134R/EYFP)Hze}$/J, Stock number: 012569, The Jackson Laboratory). Six female Thy1-ChR2-YFP mice were used for experiments involving excitatory neurons (B6.Cg-Tg(Thy1-COP4/EYFP)18Gfng/J, Stock number: 007612, The Jackson Laboratory).[25] Additionally, three male C57BL/6 J mice (Stock number: 000664, The Jackson Laboratory) of similar age were used for control experiments. Mice were given food and water ad libitum with a 12-h On–Off light cycle.

Animal surgery

Prior to imaging, a clear Plexiglas window was placed on the exposed skull as previously described.[26,27] Mice were anesthetized with isoflurane (3% induction, 1.5% maintenance, and 1.0 L/min air) and allowed 5–10 min for anesthetic transition. Buprenorphine (0.001 mL/g) was given 1 h before surgery. Body temperature was maintained at 37°C using a heating pad with rectal feedback. The eyes were well-lubricated with artificial tears. The scalp was then shaved, disinfected, and retracted to expose an area of approximately 8 mm × 8 mm over the skull. About 0.1 mL of 2% lidocaine was

applied to the scalp for analgesia. A clear Plexiglas window with pre-tapped holes was placed on the intact skull and secured with dental cement (C&B-Metabond, Parkell Inc., New York, USA). A second Plexiglas window was screwed to the first for protection and removed for imaging sessions. After surgery, mice were returned to their home cage and monitored two consecutive days. No imaging was performed during this post-operative period.

Optical intrinsic signal imaging

For experiments consisting of optogenetic PS and optical intrinsic signal imaging (Opto-OISI), four light emitting diodes (LEDs) centered at 470, 590, 617, and 625 nm (M470L3-C1, M590L3-C1, M617L3-C1, M625L3-C1, Thorlabs, NJ, USA) illuminated the skull and were interleaved with the PS laser as previously described (Figure 1(a)).[26] The incident power of
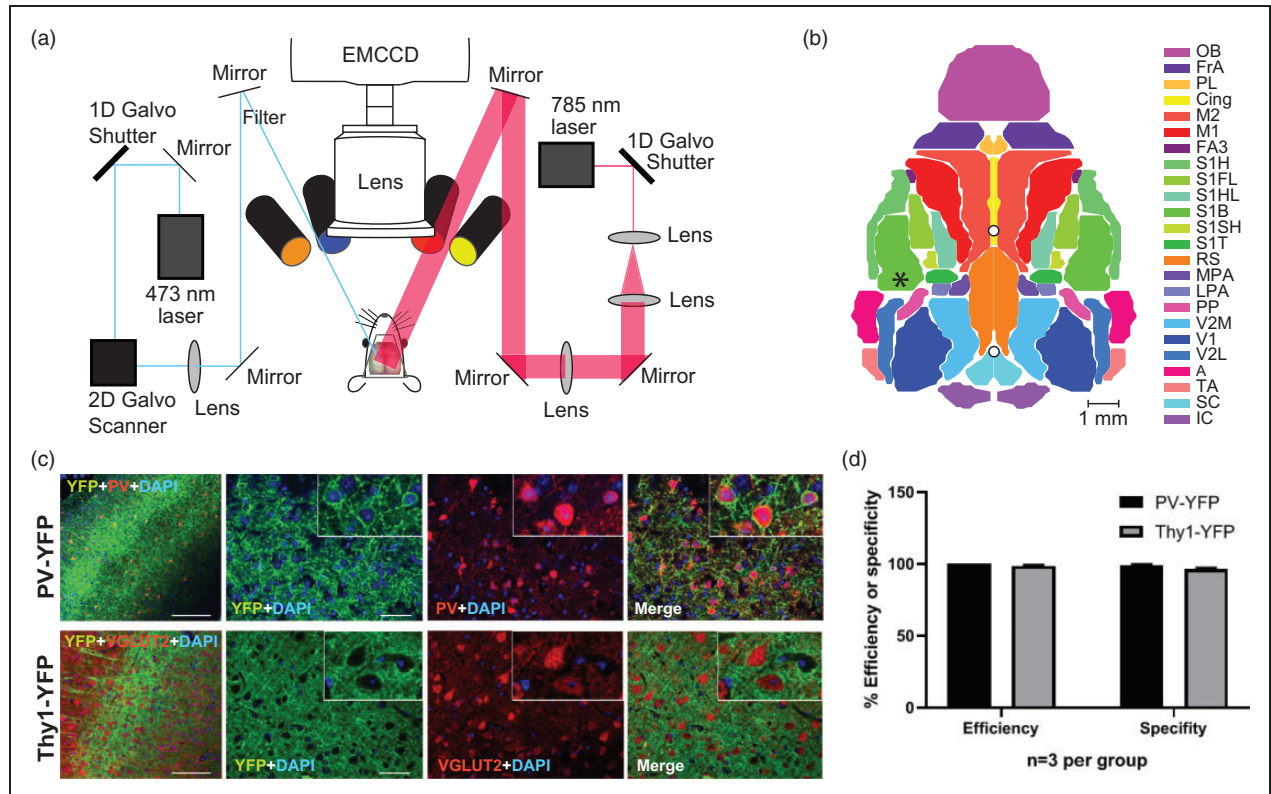

Figure 1. Optogenetic activation of hemodynamic activity in transgenic PV-ChR2 and Thy1-ChR2 mice using OISI and LSCI: (a) Opto-OISI–LSCI system. LEDs centered at 470, 590, 617, and 625 nm illuminated the skull for Opto-OIS imaging. A 473 nm laser and 785 nm laser diode were used for optogenetic targeting and LSCI, respectively. A back-illuminated EMCCD sensor collected diffuse reflected light through a 75 mm lens (f/2.8 for OISI; f/8 for OISI–LSCI). The camera's sensor was protected from laser light using a 473 nm notch filter for OISI or 530 nm high pass filter for OISI–LSCI: (b) PS was directed to left somatosensory barrel cortex (black asterisk). Photostimuli were delivered in 5 ms pulses at 20 or 10 Hz for PV or Thy1 stimulation, respectively (outside of titration experiments); (c) representative coronal slices of layers IV–VI of the somatosensory barrel. Fluorescence immunohistochemistry show expression of YFP (ChR2, green-yellow) co-localized with the PV marker (red) in the PV-ChR2 mice ($n = 3$) and VGLUT2 (also red), a pyramidal cell marker, in the Thy1-ChR2 mice ($n = 3$). Cell bodies are stained with DAPI (blue). Robust YFP expression was present in Layer 5 for Thy1 mice and a dense web of highly arborized PV-inhibitory neurons was present in Layers 2/3, 4, and 5; (d) YFP co-localization with anti-PV or anti-VGLUT2 fluorescence was examined and quantified in the somatosensory barrel cortex. Cells were counted from three sections in each mouse and measures of efficiency (% of immunolabeled neurons contain ChR2) and specificity (% of ChR2 positive neurons are immunolabeled with the respective marker) are reported. 100% of PV-immunoreactive cells and 99% of VGLUT2-immunoreactive cells expressed YFP. 99% of PV-YFP expressing neurons and 97% of Thy1-YFP expressing neurons were immunoreactive for their respective markers.
OB: olfactory bulb; FrA: frontal association; PL: prelimbic; Cing: cingulate; M2: secondary motor; M1: primary motor; FA3: frontal association area 3; S1H: primary sensory head; S1FL: primary sensory forelimb; S1HL: primary sensory hindlimb; S1B: primary sensory barrel; S1SH: primary sensory shoulder; S1T: primary sensory trunk; RS: retrosplenial; MPA: medial parietal association; LPA: lateral parietal association; PP: posterior parietal; V2M: secondary visual medial; V2L: secondary visual lateral; A: auditory; TA: temporal association; SC: superior colliculus; IC: inferior colliculus.

the 470 nm LED ($0.059 \, \text{mW/mm}^2$) was kept sufficiently below $1.3 \, \text{mW/mm}^2$ to avoid exciting ChR2.[28] We have previously tested the effect of 470 nm illumination for OIS imaging on ChR2 activation using EEG and found no discernable differences in cortical frequency content with and without 470 nm illumination.[26] An EMCCD camera (Andor iXon 897, Oxford Instruments, Oxfordshire, England) and fixed focal length lens (85 mm, f/1.4, Rokinon, New York, NY, USA) collected diffuse reflected light from the mouse's skull over a field of view of $1 \, \text{cm}^2$. Crossed linear polarizers in front of the LEDs and lens prevented specular reflections off the skull from entering the lens. The lens' f/# was set to 2.8 for all Opto-OISI experiments. A 473 nm notch filter (Chroma, ZET405/473-488/NIRm) positioned between the lens and camera prevented reflected laser light from saturating the camera's sensor. Hardware was controlled via a data acquisition card (PCI 6733, National Instruments, TX, USA) and computer (custom-built, SuperLogics, MA, USA) using custom-written software.

Opto-OISI of hemoglobin concentration changes occurred at the stimulus frequency used for each genotype (20 Hz for PV-ChR2 and 10 Hz for Thy1-ChR2). This configuration corresponded to a camera frame rate of 100 Hz for PV-stimulation and 50 Hz for Thy1-stimulation. Photostimulus frequency titration experiments interleaved the 473 nm laser with a single LED (M530L3-C1) centered at the isosbestic point of Hb to capture blood volume changes. The highest photostimulus frequency examined (100 Hz) required a camera frame rate of 200 Hz. To accommodate this speed, the camera field-of-view was reduced to 200×512 (binned 4×4 on camera). For these experiments, the laser pulse width was reduced to 4 ms to avoid temporal overlap between laser pulses and imaging frames.

Concurrent laser speckle contrast imaging and optical intrinsic signal imaging

A modified version of the system described in Bergonzi et al.[29] was used for experiments consisting of Opto-OISI with laser speckle contrast imaging (Opto-OISI–LSCI) (Figure 1(a)). The Opto-OISI component consisted of two LEDs centered at 530 and 625 nm (M530L3-C1 and M625L3-C1, Thorlabs, NJ, USA). The same camera, lens, and PS optomechanics were used as described above. For LCSI, a near-infrared laser diode (LP785-SAV50, 785 nm, 50 mW, Thorlabs, NJ, USA) was collimated to a beam diameter of 2.1 mm (F220APC-780, Thorlabs, NJ, USA) and then expanded by a factor of 5 using a Keplerian lens system to 10.5 mm to cover the skull.

According to the Nyquist sampling theorem, imaging pixels should be at least $2 \times$ smaller than the laser speckle size.[30] The speckle size is given by: $\rho_{\text{speckle}} = 2.44\lambda \, (1 + \text{M})f/\#$, where λ is the wavelength of the laser, M is the magnification of the optical system, and f/# is the f-number of the camera lens.[30] The Andor iXon 897 camera has a sensor pixel size of 16 μm. Given these specifications ($\rho_{\text{speckle}} = 32 \, \mu\text{m}$, $\lambda = 785 \, \text{nm}$, and $M = 1.2$), our aperture was set to f/8 for LSCI applications. Because the notch filter described above absorbs near-infrared light, a 515 nm long-pass filter was used to attenuate 473 nm laser light from the camera's sensor. The maximum full-field (512×512 pixels) frame rate of our camera was 30 Hz. Thus, in order to photostimulate at 20 Hz with two LEDs, one optogenetic photostimulus, and one LSCI laser, the sensor field-of-view was cropped to 200×512 pixels to allow for 80 Hz imaging at full resolution. Raw OIS data were binned offline.

Image processing

For OISI, light intensities at each wavelength (LEDs) were converted into relative changes in [HbO], [HbR], and [HbT] as we have described.[26,31] Percent change in 530 nm reflectance is reported for stimulation frequency titration experiments. For LSCI, the imaged light intensity was converted into measures of speckle contrast, K, using 5×5 kernel as outlined in Bergonzi et al.,[29] where $K = \frac{\sigma(I)}{<I>}$ (σ is the standard deviation and I is the measured intensity of the kernel). Relative measures of CBF (ΔCBF) were interpreted as $\Delta\text{CBF} = 1/K^2$. Image sequences were temporally filtered using a bandpass filter (0.009–0.25 Hz for Opto-OIS–LSCI applications or 0.009–0.5 Hz for Opto-OIS applications) as previously described.[26] The time traces for each pixel were downsampled to 1 Hz to reduce noise and data size. Quantification of some temporal signal characteristics (e.g. time-to-peak) was performed on data downsampled to 10 Hz. To increase spatial specificity of stimulus evoked responses, global signal regression was performed to remove shared variance within the field-of-view of each mouse. All image sequences were affine-transformed to a common atlas space.[32] Maps of peak ΔCBF and hemoglobin responses were generated by temporally averaging image sequences 1 s before to 1 s after stimulation offset. Time courses for pixels in peak maps having a value greater than 50% of maximum amplitude were averaged for generating response time courses. Evoked responses were censored, such that only stimulation presentations having a signal-to-noise ratio (SNR) > 1.5 were included.

Relative measures of [HbO], [HbR], and CBF were used to calculate relative changes in the cerebral

metabolic rate of oxygen consumption, $\Delta CMRO_2$, according to

$$\Delta CMRO_2 = \frac{(1 + \Delta CBF)(1 + \gamma_r \Delta[HbR])}{1 + \gamma_t \Delta[HbT]} - 1$$

where γ_r and γ_t are vascular weighting constants.[33,34] $\Delta[HbR]$ and $\Delta[HbT]$ were calculated as the ratio of the change in concentration to an assumed baseline concentration of 40 and 100 μM, respectively. Vascular weighting constants were set to 1 according to prior work.[29,34]

Photostimulation

Cortical PS was performed using a 473 nm laser (BL473T8-150, Shanghai Laser & Optics Century Company, Shanghai, China). For Experiments 1, 3, and 4 (see below), laser power was maintained at 0.5 mW (continuous wave intensity of 2.1 mW/mm^2) as previously described.[26] A 1D galvanometer was used to optically shutter the laser to deliver 5 ms pulses. Given the native fast-spiking properties of PV-expressing neurons,[15] for most experiments, PV-ChR2 mice were stimulated with 20 Hz pulses, while Thy1-ChR2 mice were stimulated with 10 Hz pulses[26] unless otherwise stated. For each mouse, the photostimulus location on the skull was registered to each mouse using bregma and lambda as landmarks (Figure 1(b)). PS parameters for titration experiments specific to Experiment 2 are described below.

Peripheral WS

Mouse vibrissae were stimulated using pressurized blasts of air. A pressure ejection system (Picospritzer III, Parker Hannifin, NH, USA) produced 40 psi pulses of air that were triggered by an external stimulation box configured to deliver a 5 s train of 100 ms pulses at 3 Hz.

Histology preparation

Mice were deeply anesthetized with FatalPlus (Vortech Pharmaceuticals, MI, USA) and transcardially perfused with heparinized PBS. The brains were removed and fixed in 4% paraformaldehyde for 24 h and transferred to 30% sucrose in PBS. After brains were saturated, they were snap-frozen on dry ice and coronally sectioned (50 μm) on a sliding microtome. Sections were stored in 0.2 M PBS, 30% sucrose, and 30% ethylene glycol at $-20°$C. ChR2 fluorescence was confirmed in each individual using epifluorescence microscopy (Nikon Eclipse 80i, Nikon Instruments Inc., New York, NY, USA). ChR2 colocalization

with PV (in PV-ChR2 animals) and excitatory marker VGLUT2 (in Thy1-ChR2 animals) was confirmed using fluorescence immunohistochemistry (Figure 1(c)).

Fluorescence immunohistochemistry

Sections containing barrel cortex were pretreated with PBS-T and blocked with 3% dry milk in PBS-T for 1 h at 25°C. Sections were incubated overnight at 4°C in 1% dry milk in PBS-T solution containing either polyclonal rabbit anti-PV antibody (1:1000, ab11427, Abcam) or monoclonal mouse anti-VGLUT2 antibody (1:1000, #832802, BioLegend, CA, USA). After three PBS washes, sections were incubated for 1 h at 37°C in either DyLight 649 conjugated AffinPure Donkey anti-rabbit IgG for PV IHC or Cy™5 AffiniPure Donkey Anti-Mouse IgG (H + L) for VGLUT2 IHC (1:800; Jackson ImmunoResearch, Pennsylvania, PA, USA). Sections were washed, mounted, and coverslipped with VECTASHIELD Antifade Mounting Medium with DAPI (Vector Laboratories, CA, USA) (Figure 1(c)).

Fluorescence microscopy and cell counting

YFP colocalization with anti-PV or anti-VGLUT2 fluorescence was examined using serial z-stack images taken on an inverted confocal microscope using a 40$\times$ oil lens objective (Nikon A1-Rsi, Nikon Instruments Inc., NY, USA). The colocalization of YFP fluorescence and immunoreactive cells was quantified manually in Imaris colocalization software (Bitplane, Switzerland, USA), using three sections per mouse, with images taken within barrel cortex (Figure 1(d)).

Statistics

All data were processed using custom-written software in MATLAB (MathWorks, MA, USA). Levels of significance ($p < 0.05$) for all pair-wise comparisons were determined using a two-tailed Students t-test assuming unequal group variance. The linear relationship between numerical variables was assessed with Pearson's correlation coefficient (MATLAB). Data visualization was performed in MATLAB, and all figures were superficially edited in Adobe Illustrator (Adobe Inc., CA, USA). Because we are not testing across different experimental groups, randomization was not performed. Experimenters were not blinded to the genotypes of the mice used.

Experimental design

Experiment 1: The role of inhibitory versus excitatory neurons on NVC. Awake Opto-OISI–LSCI determined photostimulus evoked responses of $\Delta[HbO]$, $\Delta[HbR]$, $\Delta[HbT]$,

and ΔCBF in Thy1-ChR2 ($n = 5$) and PV-ChR2 ($n = 5$). Photostimuli (5 ms pulses delivered at 20 Hz (PV) or 10 Hz (Thy1)) were targeted to left barrel cortex, and each mouse was imaged for 30 min. Photostimuli were delivered for 5 s followed by 55 s of rest and repeated in a block design (i.e. 30 presentations/mouse).

Experiment 2: Photostimulus titrations in PV-ChR2 mice. Awake Opto-OISI was used to record diffuse light reflectance in three PV-ChR2 mice following PS of left barrel cortex. Titration experiments determined the effects of stimulation frequency (0.5 mW, 4 ms pulses delivered at 20, 40, 60, 80, or 100 Hz for 5 s) and stimulation power (5 ms pulses of 0.25, 0.5, 1, or 2 mW delivered at 20 Hz for 5 s). Each parameter set was delivered in a 60 s block and presented 15×/mouse (15 min of imaging/mouse/stimulus).

Experiment 3: NVC properties of PV-based circuits under anesthesia. Opto-OISI determined photostimulus evoked ΔHbO, ΔHbR, and ΔHbT responses in PV-ChR2 mice ($n = 5$). Photostimuli consisted of 5 ms pulses delivered at 20 Hz for 5 s targeted to left barrel cortex. Imaging was performed under ketamine–xylazine (86.9 mg/kg ketamine, 13.4 mg/kg xylazine, delivered via IP injection) or isoflurane (2% induction, 1.5% maintenance, 1.0 L/min air). For imaging under isoflurane, the mouse was maintained at 1.5% for 30 min before imaging to ensure equilibrium. To accommodate lower amplitude responses under isoflurane,[35] we used 1 mW photostimuli, but 0.5 mW for awake and ketamine–xylazine conditions. Anesthetic agents were used on different days with at least one day between imaging sessions.

Experiment 4: The effect of increased local inhibition on cortical processing of peripheral input. Awake Opto-OISI was used to record cortical hemodynamic activity following WS, PS of barrel cortex only, or simultaneous WS + PS in PV-ChR2 mice ($n = 5$). Mice were imaged for 45 min split into three 15 min epochs. Epoch 1 consisted of WS only, epoch 2 consisted of PS only, and epoch 3 consisted of WS + PS. Stimuli were delivered for 5 s followed by 55 s of rest and repeated in a block design (i.e. 15 presentations/epoch/mouse).

Results

Cerebral hemodynamics are differentially regulated by Thy1- and PV-based neural circuits

To assess the efficiency and specificity of the transduction, we examined the colocalization of YFP (expressed in target neurons of the genetically manipulated mice) with immunohistochemical markers specific to the neuronal subtype. In PV-ChR2 mice, we found that YFP was expressed in 100% of neurons immunostaining for PV; PV immunostaining was present in 99% of YFP-positive neurons. Likewise, in Thy1-ChR2 mice, YFP was expressed in 99% of neurons immunostaining for VGLUT2; VGLUT2 immunostaining was present in 97% of YFP-positive neurons (Figure 1(c) and (d)).

In all mice, PS of either circuit within the left barrel cortex elicited robust and repeatable hemodynamic responses (Figure 2). PS of control mice in the same location did not produce detectable activity (Figure S1). Thy1-based circuit activation resulted in responses similar to those following peripheral stimulation characterized by increased Δ[HbO] of 3.21 μM, decreased Δ[HbR] of -0.70 μM, and increased Δ[HbT] of 2.52 μM (Figure 2(a)). In contrast, activation of PV-circuits resulted in opposite hemodynamic responses: decreased Δ[HbO] of -1.07 μM, increased Δ[HbR] of 0.30 μM, and decreased Δ[HbT] of -0.78 μM (Figure 2(b)). Peak changes differed significantly between inhibitory and excitatory stimulation (Δ[HbO]$_{Thy1}$:Δ[HbO]$_{PV}$ = -3.00, $p < 0.0001$; Δ[HbR]$_{Thy1}$:Δ[HbR]$_{PV}$ = -0.30, $p < 0.0001$; Δ[HbT]$_{Thy1}$:Δ[HbT]$_{PV}$ = -3.23, $p < 0.0005$). In addition, the relative ratios between HbO, HbR, and HbT following PS of each cell-type suggested a higher fractional weight of HbR for PV over Thy1 (Thy1: |Δ[HbO]$_{Thy1}$:Δ[HbT]$_{Thy1}$:Δ[HbR]$_{Thy1}$| = 4.6:3.6:1, PV: |Δ[HbO]$_{PV}$:Δ[HbT]$_{PV}$:Δ[HbR]$_{PV}$| = 3.6:2.6:1) (Figure 2(c) to (f)). The time-to-peak response for PV was delayed approximately 1 s across hemodynamic measures in comparison to those of Thy1 (Figure 2(e) and (f)). Spatially, peak PV hemodynamic responses encompassed a larger area than those of Thy1 activity ($p < 0.005$) (Figure 2(c) to (f)). Maps of diffuse reflectance in representative animals are shown in Figure S2.

Increased PV activity decreases CBF and CMRO$_2$

"Negative" hemodynamic activity consistently followed each photostimulus train across all tested awake PV-ChR2 mice. While reduced CBV in the presence of reduced oxygenation could indicate neuronal inhibition,[36] the sign and magnitude of BOLD signals depends on the relative changes in CBF and the cerebral metabolic rate of oxygen consumption, CMRO$_2$.[37–39] As shown in Figure 2, excitatory stimulation resulted increased local ΔCBF (7.94%) in left barrel cortex for Thy1-ChR2 PS (Figure 2(a) and (c)) and decreased ΔCBF (-3.30%) in PV-ChR2 mice (Figure 2(b) and (d)). Because ΔCMRO$_2$ depends on local ΔCBF and available oxygen,[34] we hypothesized that increased PV activity would result in reduced tissue averaged oxygen consumption. We estimated ΔCMRO$_2$ using measured Δ[HbR], Δ[HbT], and
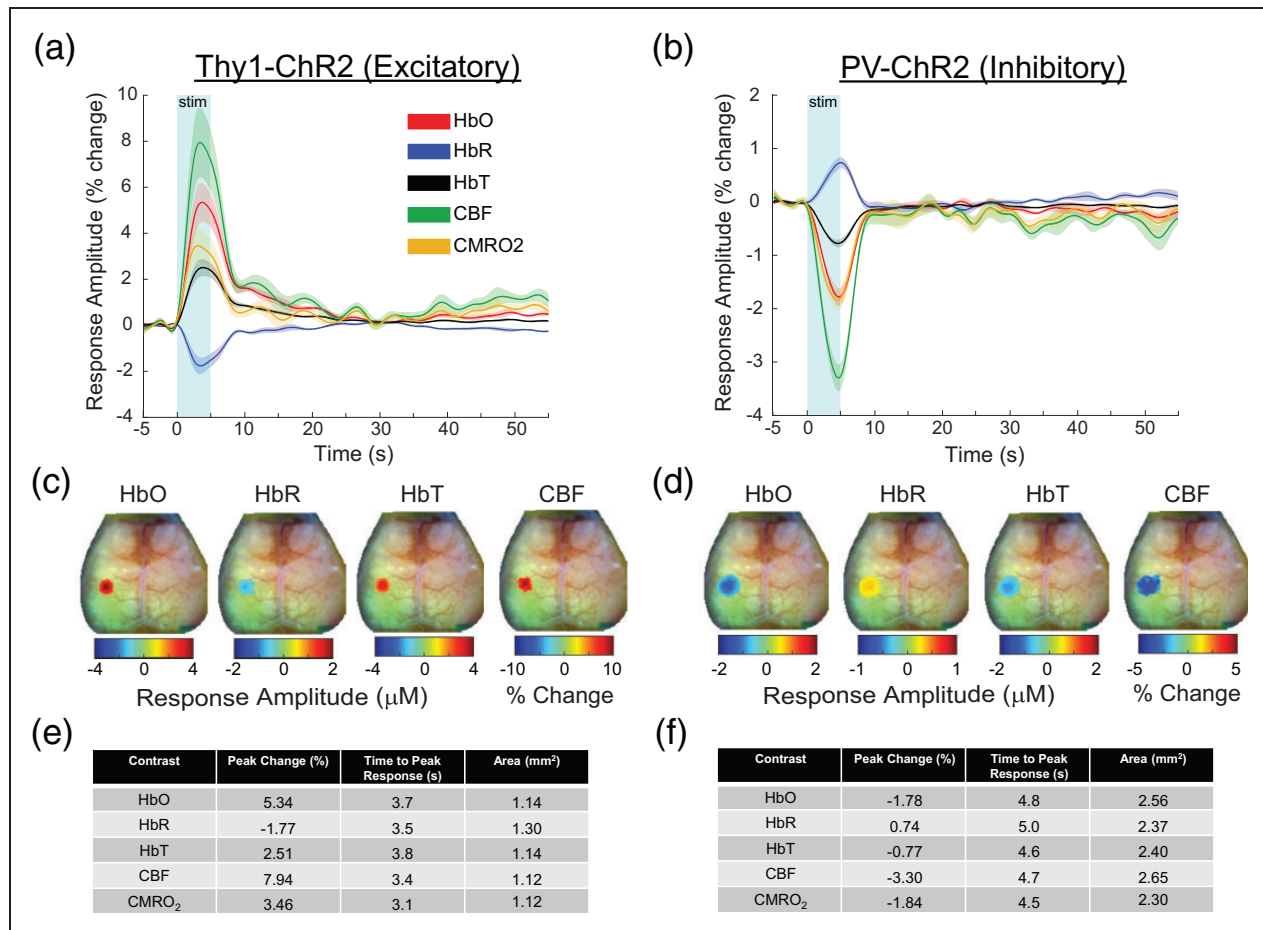
Figure 2. Excitatory and inhibitory circuits differentially regulate local cerebral hemodynamics. (a,b) Photostimulus-evoked activity in barrel cortex of HbO, HbR, HbT, CBF, and $CMRO_2$ in (a) Thy1-ChR2 ($n = 5$) or (b) PV-ChR2 ($n = 5$) mice. Activation of Thy1 circuitry consistently produced increases in HbO, HbT, CBF, and $CMRO_2$. PS of PV-based circuits consistently induced decreases in HbO, HbT, CBF, and $CMRO_2$. PS consisted of 5 ms pulses of 0.5 mW 473 nm light delivered at 10 Hz (Thy1) or 20 Hz (PV) for 5 s. The group-averaged time courses were determined by thresholding peak $\Delta[HbT]$ maps (e.g. Figure 2(c)) at 50% of max and averaging all time courses in pixels above that threshold. All time traces were censored, such that only stimulus-evoked time traces with SNR > 1.5 were included (Thy1-ChR2: 82% of stimulation presentations and PV-ChR2: 92% of stimulation presentations). $CMRO_2$ was estimated from time traces of [HbO], [HbR], and CBF. Peak onset for each signal followed shortly after the start of stimulation (time to 50% of $\Delta[HbT]$ peak: (a) 1.5 and (b) 2.0 s), returning to baseline with similar kinetics. No significant deviations from baseline were measured throughout the 55 s rest period; (c,d) peak maps for $\Delta[HbO]$, $\Delta[HbR]$, $\Delta[HbT]$, and ΔCBF. Maps were averaged from one second before and after stimulation ended. Responses in left primary somatosensory barrel cortex are centered on the site of PS. Pixels exhibiting responses larger than 50% of max amplitude are shown on a white light image of the mouse skull from our imaging camera. As with (a,b), only stimulation-evoked activity having SNR > 1.5 are included. Surrounding regions were near-zero and showed no significant deviations from baseline measures. For both Thy1 and PV maps, local changes in [HbO], [HbR], [HbT], and CBF were positive or negative throughout the entire area of response. See Supplemental Figure 2 for images of raw light reflectance; (e,f) quantitative characterization of responses reported in (a–d). [HbO], [HbR], [HbT], and CBF responses were approximately 2–3 × larger in Thy1-ChR2 mice versus PV-ChR2 mice, while the area of peak response was 2 × larger for PV-ChR2 mice. Additionally, time to peak was approximately 1 s longer in PV-ChR2 mice compared to Thy1-ChR2 mice.

ΔCBF. $\Delta CMRO_2$ increased during stimulation of excitatory neurons (3.46% in Thy1-ChR2 mice) (Figure 2(a)) but decreased during stimulation of inhibitory neurons (−1.84% in PV-ChR2 mice) (Figure 2(b)). The temporal dynamics of $\Delta CMRO_2$ with increased excitatory activity closely matched previous reports

characterized by a peak onset (3.1 s) leading both ΔCBF (3.4 s) and Δ[Hb] (3.5–3.8 s) (Figure 2(e)).[34]

The magnitude of negative, PV-based hemodynamic activity depended on stimulation frequency and photostimulus power (Figures 3 and S3). Titrating photostimulus frequency with fixed power (0.5 mW) resulted in a
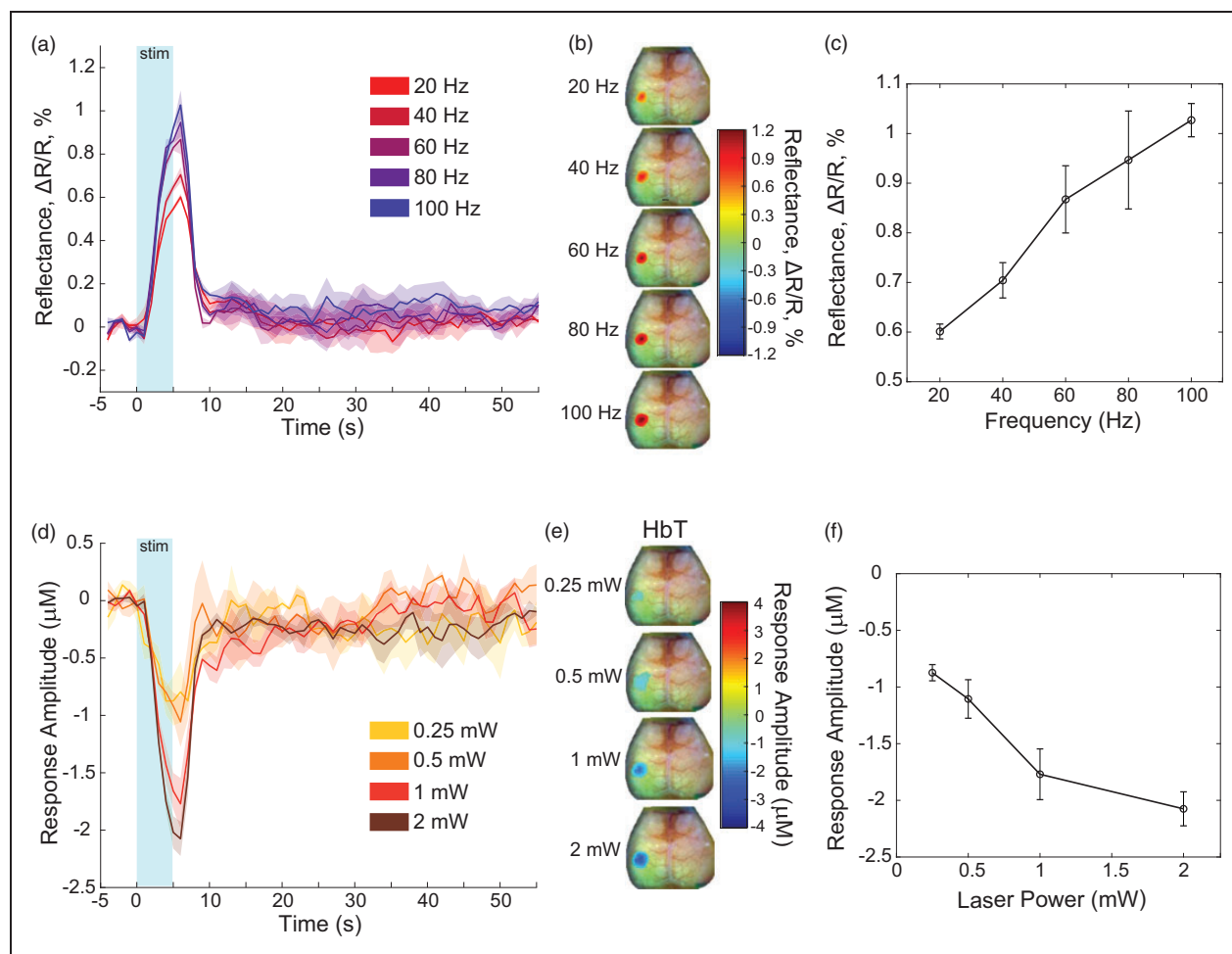
Figure 3. Magnitude but not sign of ChR2-evoked hemodynamic activity in PV-ChR2 mice depends on PS parameters. For panels (a–c), a single LED centered at 530 nm (the isosbestic point of Hb) was used to capture changes in light reflectance that are independent of oxygenation and proportional to changes in cerebral blood volume or [HbT]: (a) time course of diffuse reflectance from left barrel cortex during PS frequency titrations in three mice. Time traces were generated by thresholding peak Δ[HbT] maps (e.g. Figure 3(b)) at 50% of max and averaging all time courses in pixels above that threshold. Five frequency settings were tested (in Hz: 20, 40, 60, 80, and 100) that spanned the native fast-firing rates of PV-expressing interneurons. Only reflectance time traces with an SNR > 1.5 were included (98, 100, 98, 98, and 96% of all stimulus presentations at 20, 40, 60, 80, and 100 Hz, respectively). Increases in reflectance during stimulation indicate less light absorption due to decrease in blood volume. Higher frequencies elicited larger increase in peak response; (b) peak reflectance maps for each frequency setting. Maps were temporally averaged from 1 s before and after stimulus ended and thresholded to show pixels above 50% of maximum response; (c) line-plot showing % change in peak reflectance for each frequency setting. An approximately direct, linear relationship was observed between % change in reflectance and frequency ($r = 0.99$, $p < 0.005$); (d) Δ[HbT] time-traces across different photostimulus power settings (0.25, 0.5, 1, and 2 mW). Time-traces were generated by averaging across pixels shown in 50% of max thresholded response maps at the mouse-level (e.g. Figure 3(e)). With higher power settings, we observed larger decreases in Δ[HbT]. Time-traces exhibited higher SNR with higher photostimulus power (number of traces with SNR > 1.5: 44% for 0.25 mW data, 67% for 0.5 mW data, 89% for 1 mW data, and 98% for 2 mW data); (e) peak Δ[HbT] maps across power settings. Maps were temporally averaged from 1 s before to 1 s after the end of stimulation and thresholded to show pixels above a 50% of max response. In general, higher photostimulus power elicited increases in Δ[HbT] as well as larger local areas of response; (f) line-plot depicting peak Δ[HbT] across different power settings. An approximately direct, linear relationship was observed between [HbT] response amplitude and laser power ($r = -0.95$, $p < 0.05$). Δ[HbO], Δ[HbR], and Δ[HbT] time traces and peak maps are reported in Supplementary Figure 3.

monotonic increase in peak reflectance (Ref20$_{Hz}$: Ref40$_{Hz}$:Ref60$_{Hz}$:Ref80$_{Hz}$:Ref100$_{Hz}$ = 0.60%:0.70%: 0.87%:0.95%:1.03%; Pearson R = 0.99, p < 0.05) signifying graded decreases in CBV (Figure 3(a) to (c)).

Titrating photostimulus power with fixed frequency (20 Hz) resulted in monotonic decreases in CBV with increasing laser power (Δ[HbT]$_{0.25mW}$:Δ[HbT]$_{0.5mW}$:Δ[HbT]$_{1mW}$:Δ[HbT]$_{2mW}$ = −0.87%:−1.11%:−1.77%:

−2.08%; Pearson R = − 0.95, p < 0.05) (Figures 3(d) to (f) and S3).

Anesthesia affects the sign and magnitude of PV-based hemodynamic responses

Anesthesia is known to affect both spontaneous and stimulus evoked brain activity. The use of anesthesia in several studies examining cellular contributions to NVC motivated us to explore whether the observed negative hemodynamic responses following PV stimulation persisted under common anesthetic agents, isoflurane and ketamine–xylazine. Each PV-ChR2 mouse was photostimulated while awake prior to the administration of either agent as a control (Figure 4(a)). Following injection of ketamine–xylazine, cortical responses were negative and appreciably smaller (48%, p < 0.005) compared to awake responses (Figure 4(b)). Peak response area was similar across conditions (p = 0.21).

A more complicated picture was observed under different levels of isoflurane. Under 1% isoflurane, photostimulus evoked hemodynamic responses were negative (Δ[HbO]: −0.90 μM, Δ[HbR]: 0.32 μM, Δ[HbT]: −0.58 μM) (Figure 4(c)) and did not significantly differ from awake responses (p = 0.43 for peak Δ[HbO]$_{awake}$:Δ[HbO]$_{1\% iso}$, p = 0.98 for peak Δ[HbR]$_{awake}$: Δ[HbR]$_{1\% iso}$, p = 0.20 for peak Δ[HbT]$_{awake}$:Δ[HbT]$_{1\% iso}$). Response area was also similar to awake responses (p = 0.49). However, under 1.5% isoflurane, PV PS resulted in increase of Δ[HbO] and Δ[HbT] and decrease of Δ[HbR], i.e. responses more in line with typical functional hyperemia (Figure 4(d)). Peak signal changes of Δ[HbT] were approximately 42% smaller in magnitude than the awake case (p < 0.00001), while the spatial extent of these responses was approximately 50% smaller than in awake mice (p < 0.005) (Figure 4(f)).

Anesthesia also had a profound effect on the response dynamics (Figure 4(e)). In awake mice, response onset (time to 10% of peak) was 0.6 s:1.1 s: 0.4 s (Δ[HbO], Δ[HbR], Δ[HbT]), and the time-to-peak was 4.8 s:5.0 s:4.6 s (Δ[HbO], Δ[HbR], Δ[HbT]). These response characteristics were delayed in both ketamine–xylazine anesthetized mice (onset: 1.8 s:1.3 s:1.5 s; time to peak: 5.8 s:6.0 s:5.6 s) and mice anesthetized with 1.5% isoflurane (onset: 1.4 s:3.1 s:1.3 s; time to peak: 7.1 s:7.9 s:7 s) for Δ[HbO], Δ[HbR], and Δ[HbT], respectively.

PV circuits mediate cortical excitation during peripheral stimulation

Because inhibitory interneurons are known to play a significant role in moderating and fine-tuning excitatory activity,[40] we examined how PV circuits altered hemodynamic activity associated with cortical processing of peripheral input. WS in PV-ChR2 mice produced localized increase in Δ[HbO] and Δ[HbT] and decrease in Δ[HbR] as expected (Figure 5(a), WS). Optogenetic targeting of left somatosensory barrel cortex reproduced negative hemodynamic responses (Figure 5(a), PS). However, simultaneous delivery of these two stimuli significantly decreased Δ[HbO] by 30% (p < 0.05) and trended toward increased Δ[HbR] (34%, p = 0.14) and decreased Δ[HbT] (27%, p = 0.2) compared to WS alone (Figure 5(b)).

Discussion

Understanding cellular contributions to local changes in hemodynamic activity is essential for interpreting blood-based brain imaging signals and might allow for predicting underlying neural circuitry producing these responses.[41] While increased activity in excitatory and inhibitory neurons has been shown to result in increased CBF, less examined has been the role of specific subpopulations of interneurons in regulating the brain's blood supply. We examined the role of PV interneurons, the largest subpopulation of GABAergic cells, in NVC. Compared to excitatory activity, increased PV activity reduced oxygenation and decreased CBV and CBF. These negative PV-based hemodynamic responses were consistent within and across mice and were highly reproducible across a broad range of photostimulus parameters. However, the sign and magnitude of the hemodynamic response resulting from PV activity was highly dependent on the type and level of anesthesia used. Our findings build off of previous work demonstrating cell-specific contributions to NVC[3,4,7,10,12–14,39,42] and highlight a critical role of PV interneurons in this process.

Excitatory and inhibitory circuits differentially regulate local hemodynamic and metabolic responses

Optogenetic targeting of PV-expressing neurons in awake mice elicited hemodynamic activity consistent with local inhibition of neural activity and findings harmonious with what has been described in the fMRI literature as a negative BOLD signal.[36,39,43–45] Because PV interneurons are fast spiking and energy demanding,[40,46] direct activation of PV cells alone might be expected to result in increased CBF, CBV, and CMRO2.[42] However, the amplitude and polarity of BOLD signaling in the brain depends on the relative changes in CBF and CMRO$_2$.[37–39] For a brain region to exhibit a negative BOLD response, local [HbR] must increase,[38] which can be achieved through several
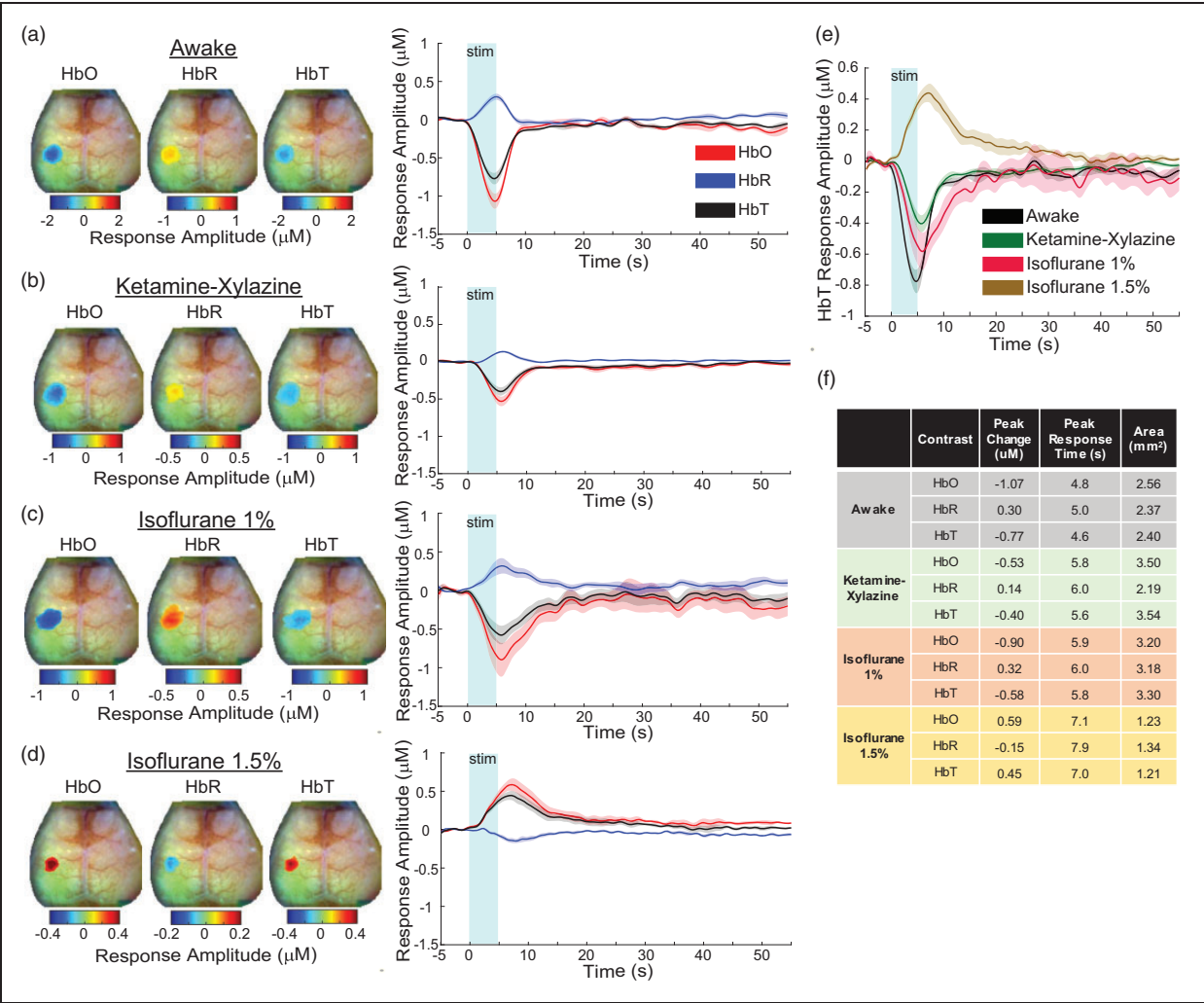
Figure 4. Cortical hemodynamics following increased PV activity is differentially modulated by anesthesia: (a) peak maps and time traces of Δ[HbO], Δ[HbR], and Δ[HbT] generated by PS (473 nm 0.5 mW light delivered at 20 Hz as 5 ms pulses) of PV circuits in awake mice ($n = 5$). Maps were averaged from 1 s before to 1 s after end of PS and thresholded to show pixels 50% or greater of max amplitude within the local region. Time traces were generated by averaging pixel time traces within the thresholded region of each contrast's peak maps. Only time courses with an SNR > 1.5 are included (92% of stimulation presentations); (b) peak maps and corresponding time courses (95% of stimulus presentations with SNR > 1.5) measured during PS (parameters identical to panel (a)) of PV circuits ($n = 5$) under ketamine (86.9 mg/kg)–xylazine (13.4 mg/kg) anesthesia. The sign of the responses was the same as observed in awake mice; however, peak response magnitudes were reduced by approximately 50%, and the response area increased by 50%; (c) peak maps and time courses (66% of stimulus presentations with SNR > 1.5) measured during PS (parameters identical to panel (a)) of PV circuits ($n = 5$) under 1% isoflurane anesthesia (1 L/min air). Responses are similar to those observed in awake mice, characterized by decreases in Δ[HbO] and Δ[HbT] and increases in Δ[HbR]. The FWHM area of effect was similar in size to the response under ketamine–xylazine anesthesia in panel (b). A 1 mW laser power was used in this data-set to account for lower SNR in cortical responses measured during isoflurane imaging; (d) peak maps and time courses (80% of stimulus presentations with SNR > 1.5) measured during PS of PV circuits ($n = 5$) under 1.5% isoflurane (1 L/min air) result in responses consistent with normal functional hyperemia. In all mice examined, the sign of the evoked response in Δ[HbO], Δ[HbR], and Δ[HbT] was opposite to those measured in awake mice and anesthetized mice under ketamine–xylazine or isoflurane 1%. Note that responses in (d) were also recorded using 1 mW stimulus presentations like panel (c) to accommodate a lower SNR in cortical responses. All other photostimuli parameters were consistent with that of panels (a–c); (e) summary of Δ[HbT] time-traces for each imaging condition from panels (a–d). Of note, use of anesthesia in general resulted in lagged time-to-peak compared to awake responses (∼6 s under ketamine–xylazine, ∼6 s under 1% isoflurane, and ∼7 s under 1.5% isoflurane); (f) quantification of response characteristics for all contrasts.
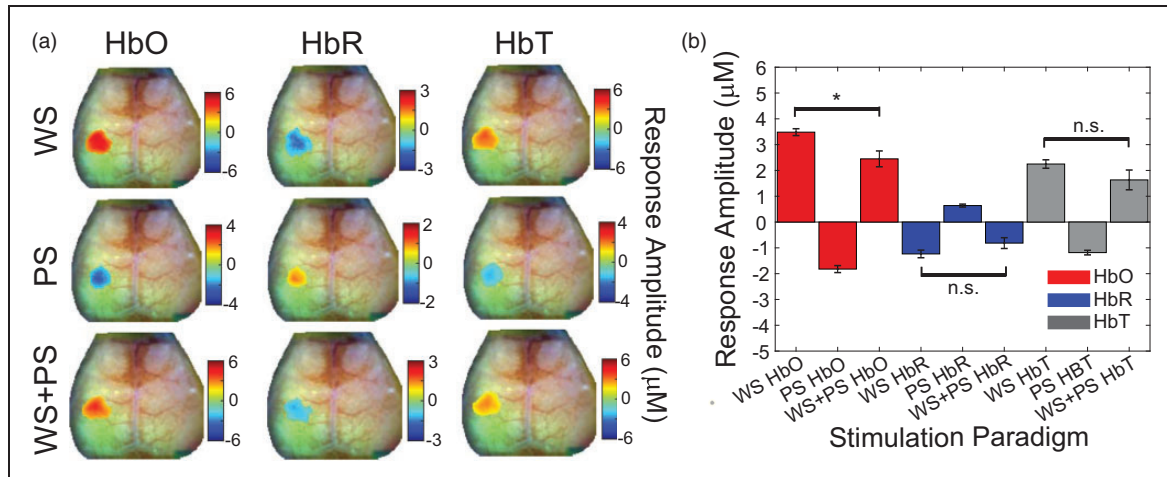
Figure 5. Increased PV activity reduces local available oxygen during peripheral stimulation. A picospritzer delivered pressurized blasts of air (40 psi) at 3 Hz to the right vibrissae in order to drive activity in the left barrel cortex ($n = 5$). Photostimuli (473 nm 0.5 mW light delivered at 20 Hz as 5 ms pulses) were also targeted to the left barrel cortex. Three experimental conditions were examined, WS alone, PS alone, and simultaneous WS and PS (WS + PS) over a 5 s stimulation period: (a) Δ[HbO], Δ[HbR], and Δ[HbT] peak maps for each experimental condition were averaged from 1 s before to 1 s after the end of stimulation. Maps were thresholded to show pixels 50% or greater than the max amplitude within the local region. All conditions resulted in well-localized responses. As expected, WS only resulted in normal functional hyperemia within barrel cortex, while PV activity alone resulted in the opposite response profile. Combining WS + PS resulted in qualitatively lower peak responses compared to WS alone; (b) quantification of peak hemodynamic response across conditions. Each bar represents an average for the respective contrast/condition of pixels within the masked region in (b). Significantly reduced local oxygenation was observed during simultaneous WS and PS compared to WS alone (30% decrease, $p < 0.05$), indicating that increased PV activity reduced local excitation due to cortical processing of peripheral input. n.s.: not significant, *$p < 0.05$.

mechanisms: (1) increased CBV or $CMRO_2$ absent any corresponding increases in CBF, (2) larger decreases in CBF compared to $CMRO_2$, (3) larger increases in $CMRO_2$ compared to CBF, or (4) comparable decreases in CBF and $CMRO_2$.[40,46] Local energetics in combination with the structural and functional connectivity of the driven circuit determine the local response. Anatomically, PV interneurons are primarily composed of basket and chandelier cells that exhibit multipolar dendrites and expansive axonal arborizations,[40] which preferentially synapse on to pyramidal neurons.[47,48] Functionally, these cells are the primary source of lateral and feed-forward inhibition in barrel cortex.[49] Our data suggest that increased PV activity reduces CBF to a greater extent than $CMRO_2$, in line with mechanism #2 above.[36,50] $CMRO_2$ has been hypothesized to represent the energy budget required for reestablishing ion gradients following depolarization.[13,51–53] We interpret the observed negative BOLD signaling and $CMRO_2$ reduction as evidence of PV-induced decreases in local, spontaneous excitatory activity. Widespread downstream inhibition of pyramidal cell activity following PV stimulation reduces oxygen demand within this network, and at the tissue level, these reductions outweigh increases otherwise expected from the photostimulated PV-interneurons.

PV cells exhibit dense connectivity onto pyramidal cells and each other via electrical gap junctions and synapses, extending a blanket of inhibition on local excitatory activity.[54–59] This expansive connectivity might explain why photostimulus evoked hemodynamics in PV-ChR2 mice was approximately $2 \times$ larger in area than those in Thy1-ChR2 mice. L5 pyramidal neurons have pronounced apical dendritic tufts in L1 and L2/3.[60,61] Thy1 PS results in activity originating in L5 that propagates to L2/3 and then L4 near the stimulation site ($<200 \mu m$).[62] Distant activity ($>500 \mu m$) spreads horizontally and is mostly restricted to L2/3,[62,63] where pyramidal neurons exhibit widespread lateral connectivity.[64] PV cells are found in all cortical layers except L1.[65] Combined, PV silencing of widespread lateral excitatory projections and activation of other proximal PV interneurons results in large spatial patterns of reduced hemodynamic activity. This observation is in accordance with a recent study in which we observed a larger-than-expected spatial spread of calcium activity following chemogenetic manipulation of PV circuits.[56] In the present study, PV PS also significantly reduced evoked hemodynamic activity during peripheral WS. A recent study reported during a similar experiment that evoked gamma band LFP amplitudes in barrel cortex during combined PV and WS

were half as large as those induced by WS alone.[13] Collectively, these observations support the biological role of PV cells in mediating local excitation[40] and are in line with other literature reporting a negative correlation between elevated GABA levels and BOLD response amplitude.[66,67]

Reductions in CBF and oxygenation observed following PV stimulation corroborate previous findings reporting PV-induced vasoconstriction in brain tissue slices.[8] The neocortex and thalamus also contain PV-positive pyramidal cells in small populations.[68] Numerous studies, including our own, have shown that driving pyramidal cell activity induces a positive BOLD response,[26,62,69–72] while neural deactivation has been linked to the negative BOLD signal.[36,43,73] The increase in Δ[HbR] following PV-ChR2 stimulation suggests that the response we observe is predominantly due to driving inhibitory interneurons rather than a small number of PV-expressing pyramidal cells.

Negative hemodynamic responses elicited by PV PS emphasize the importance of investigating the role of specific interneuron subpopulations in NVC. Optogenetic targeting of VGAT-expressing cells has shown increase in CBF and biphasic changes in vessel diameter.[9–11] However, because VGAT is present in most GABAergic cells, the resulting hemodynamic response following VGAT PS represents the cumulative result of increased activity in nearly all interneurons. This lack of targeting specificity makes it difficult to parse the roles of a particular subgroup of cells responsible for dilation and/or constriction phases of the vascular response. We observed an immediate decrease in CBF of approximately 3% when PV cells are stimulated. Others have reported an approximate 20% increase in CBF following VGAT stimulation.[9] These opposed signals temporally overlap; vasodilatory influences of VIP- and NOS-expressing neurons[12] could outweigh the apparent vasoconstriction observed following increased PV activity.[3,4,10]

PV-driven hemodynamic activity depends on arousal and anesthesia dose

Without electrophysiological data, it is difficult to explain these dose-dependent changes in signal polarity. Instead, we offer the following speculations considering the mechanism of action of each anesthetic and its effect on baseline CBF.

Ketamine acts primarily as an NMDA receptor antagonist and thus lowers excitatory activity globally over the cortex, without alter resting CBF.[74] Synaptic activity between PV interneurons and excitatory cells might be relatively preserved under ketamine–xylazine. However, because excitatory activity is lowered, the net effect of PV-induced inhibition could be smaller.

These factors might explain the comparatively lower hemodynamic responses under ketamine–xylazine compared to awake responses.

Isoflurane depresses excitatory transmission through inhibition of glutamate release and NMDA receptors,[75–78] while potentiating GABA-A receptors dose-dependently.[79–82] At lower concentrations, resting CBF and CBV are not appreciably affected by isoflurane.[83,84] However, at higher doses, isoflurane has been shown to increase baseline CBF via vasodilation of pial arteries,[36,83] which can have a dramatic effect on stimulus evoked hemodynamics.[84,86] While dilated vessels might be expected to exhibit smaller stimulus-driven changes in diameter,[85] task-driven CBF responses are highly dependent on isoflurane dose and stimulus frequency delivered.[75,86] For example, CBF responses in the rat from single pulse stimuli are approximately $3\times$ higher at 2.1% isoflurane compared to 1% (see Figure 3 in Masamoto et al.[75]). The influence of PV-induced decreases in CBF could be differentially dampened by baseline changes in CBF dependent on isoflurane concentration.

Dose-dependent effects of isoflurane on resting vascular diameter might not feature prominently in PV-induced hemodynamic activity. Responses under 1% isoflurane were similar in magnitude and sign to those while awake, which could indicate that the experimental groups are in similar states of arousal. While isoflurane results in increased inhibition, this level of anesthesia in mice is light; mice responded to a gentle toe pinch even after 1 h of continuous exposure. Mice did not respond to a toe pinch under 1.5% isoflurane. Because isoflurane directly suppresses cortical activity,[80] optogenetically driven PV activity might not result in additional circuit-level suppression of excitatory activity. Thus, the positive responses observed under 1.5% isoflurane could be reflecting direct energetic demands of driven PV cells. Some complications attend this conclusion. PV interneurons are not known to co-express any vasoactive compounds that produce constriction (e.g. NPY, SOM) or dilation, (e.g. VIP, NOS).[4,10,12,23] However, PV interneurons are directly connected to many of these interneuron subtypes. If our observed responses under 1.5% isoflurane are not due to vasoactive messaging from downstream targets of PV cells, then the positive responses might be a result of metabolic by-products (e.g. CO_2, lactate) released from PV neurons during stimulation.

Comparisons to other studies driving PV activity

Our observed responses in mice anesthetized with 1.5% isoflurane are supported by results in Lee et al.[24] They report a PV-induced focal positive BOLD response (i.e. decreased Δ[HbR]) in isoflurane-anesthetized rats[24]

under similar doses (1.3–1.5%) and stimulation parameters (20 Hz, 7.5 ms pulses) as the mice in our study. That study also observed negative BOLD signaling in deeper brain regions flanking the site of PS. We did not observe these flanking signals, possibly because they were outside of (deeper than) our field-of-view or because of differences in photostimulus power used (6 mW in Lee et al.[24] vs. 1 mW in ours).

A more recent study by Krawchuck et al.[14] examined the role of several different subpopulations of interneurons on regulating cerebral hemodynamics over a range of photostimuli (frequencies (Hz): 5, 10, 20, and 40; pulse widths (ms): 2, 10, and 30) in awake mice using viral vectors.[14] In PV-Cre mice, Krawchuk et al.[14] reported atypical CBF responses peaking 14–18 s after stimulation offset. Interestingly, though not specifically commented upon, apparent decreases in CBF occur during the stimulus window for 5 Hz stimuli (see Figures 4 and 5 in Krawchuk et al.[14]), in agreement with our awake results. Other recent evidence by Dahlqvist et al.[13] reported increased CBF and tissue oxygen partial pressure (via oxygen polarography) following PS (2 mW, 7.5 ms pulses delivered at 100 Hz for 15 s) of PV interneurons in transgenic mice anesthetized with ketamine/xylazine and alpha-chloralose.[13] CBF increased by 3% during the stimulation with larger (~10%) changes 30 s after stimulus offset. While alpha-chloralose is not known to cause significant vasodilation like isoflurane, both share a common mechanism as GABA-A agonists that might influence similarly downstream excitatory targets. In this case, our positive responses under 1.5% isoflurane would be in agreement with those of Dahlqvist et al.[13] during their photostimulus window. While the use of anesthesia may explain discrepancies between our awake and their anesthetized findings, underlying mechanisms of specific anesthetic agents is not fully understood, and local versus tissue-averaged responses could differ. Differences in animal preparation might also explain discrepancies across studies. Craniotomies (performed in both studies) and/or the use of viral vectors have several important drawbacks, including potential damage to the cortex, toxic overexpression of ChR2, scarring within the imaging ROI from the viral injection, and potential inflammation of the cortex following skull removal. Because we explore several stimulation parameters, states of arousal, and imaging modalities through the intact skull, our findings should more realistically depict how PV interneuron activity relates to local hemodynamics. Our novel findings of PV's role in NVC support the need to further investigate how different cell populations drive local and global hemodynamics, an area of research becoming increasingly popular.[12–14]

Limitations of the current study

Clear limitations include the lack of direct measurements of neural activity (e.g. electrophysiology or calcium imaging). The combination of our imaging methods with other (non-hemodynamic) modalities would better inform how our observed hemodynamic responses relate to local network activity and metabolic demand. For example, PV stimulation clearly reduced local CBF and $CMRO_2$. If this reduction in CBF is sufficient to become rate limiting to $CMRO_2$, prolonged PV stimulation could be inducing partial ischemia.[87] An ischemia-like state would lead to increased nonoxidative glucose consumption to maintain energy-consuming processes which could be measured with 2-deoxyglucose autoradiography.[88]

Wide-field OISI and LSCI capture tissue-averaged hemodynamics resulting from ensemble neural activity. This constraint, along with the relatively low depth penetration of visible wavelengths in tissue, makes it difficult to parse layer-specific activity from superficial optical stimulation of PV cells. Given that PV interneurons are present in all cortical layers except L1, measured responses can result from both orthodromic (dendrite to soma/axon) as well as antidromic (axon to soma/dendrite) activation.[89] The lack of co-expression between PV cells and other vasoconstrictive messengers suggests that these responses result from multisynaptic communication between photostimulated cells and their local network. The use of pharmacological blockers could assist in determining the molecular pathways incorporated by PV interneurons to induce vasoconstriction.

One topic left unaddressed in this paper concerns recent reports of PV-positive cells exhibiting transcallosal axonal connectivity in the primary motor, auditory, and visual cortices.[90] It is certainly interesting that in our study, local PV stimulation can result in unilateral and possibly bilateral responses especially following higher amplitude stimuli (Figure S3). Transcallosal connectivity as observed by Rock et al.[90] has not yet been noted in the barrel cortex by other studies, including our own.[56] Whether the bilateral responses in the current paper are mediated mono or polysynaptically was left undetermined and considered to be beyond the scope of this work.

well as the McDonnell Center for Systems Neuroscience (AQB).

Declaration of conflicting interests

The author(s) declared no potential conflicts of interest with respect to the research, authorship, and/or publication of this article.

Authors' contributions

JHL and AQB conceived and designed the project. JHL performed analysis and results were interpreted by JHL and AQB. JHL, CLS, and ARB acquired the data and performed animal surgeries, while ARB managed mouse breeding. PY and ZPR performed histology, immunofluorescence, fluorescence microscopy, and cell counting. JHL and AQB wrote the initial draft of the paper with input and approval from all authors: JHL, CLS, ARB, ZPR, PY, AZS, JML, and AQB. AQB provided technical resources and supervised all aspects of the study.

Supplementary material

Supplemental material for this article is available online.

References

1. Raichle ME and Mintun MA. Brain work and brain imaging. *Annu Rev Neurosci* 2006; 29: 449–476.
2. Iadecola C. The neurovascular unit coming of age: a journey through neurovascular coupling in health and disease. *Neuron* 2017; 96: 17–42.
3. Cauli B and Hamel E. Revisiting the role of neurons in neurovascular coupling. *Front Neuroenerget* 2010; 2: 9.
4. Cauli B, Tong XK, Rancillac A, et al. Cortical GABA interneurons in neurovascular coupling: relays for subcortical vasoactive pathways. *J Neurosci* 2004; 24: 8940–8949.
5. Hamel E. Cholinergic modulation of the cortical microvascular bed. *Prog Brain Res* 2004; 145: 171–178.
6. Lecrux C and Hamel E. Neuronal networks and mediators of cortical neurovascular coupling responses in normal and altered brain states. *Philos Trans R Soc Lond B Biol Sci* 2016; 371: 20150350.
7. Lecrux C, Toussay X, Kocharyan A, et al. Pyramidal neurons are "neurogenic hubs" in the neurovascular coupling response to whisker stimulation. *J Neurosci* 2011; 31: 9836–9847.
8. Urban A, Rancillac A, Martinez L, et al. Deciphering the neuronal circuitry controlling local blood flow in the cerebral cortex with optogenetics in PV:Cre transgenic mice. *Front Pharmacol* 2012; 3: 105.
9. Anenberg E, Chan AW, Xie Y, et al. Optogenetic stimulation of GABA neurons can decrease local neuronal activity while increasing cortical blood flow. *J Cereb Blood Flow Metab* 2015; 35: 1579–1586.
10. Uhlirova H, Kilic K, Tian P, et al. Cell type specificity of neurovascular coupling in cerebral cortex. *Elife* 2016; 5: e14315.
11. Vazquez AL, Fukuda M and Kim SG. Inhibitory neuron activity contributions to hemodynamic responses and metabolic load examined using an inhibitory optogenetic mouse model. *Cereb Cortex* 2018; 28: 4105–4119.
12. Lee LM, Boorman L, Glendenning E, et al. Key aspects of neurovascular control mediated by specific populations of inhibitory cortical interneurons. *Cereb Cortex* 2020; 30: 2452–2464.
13. Dahlqvist M, Thomsen K, Postnov D, et al. Modification of oxygen consumption and blood flow in mouse somatosensory cortex by cell-type-specific neuronal activity. *J Cereb Bloof Flow Metab*. Epub ahead of print 23 October 2019. DOI: 10.1101/651224%J bioRxiv.
14. Krawchuk MB, Ruff CF, Yang X, et al. Optogenetic assessment of VIP, PV, SOM and NOS inhibitory neuron activity and cerebral blood flow regulation in mouse somatosensory cortex. *J Cereb Blood Flow Metab*. Epub ahead of print 16 August 2019. DOI: 271678X19870105.
15. Rudy B, Fishell G, Lee S, et al. Three groups of interneurons account for nearly 100% of neocortical GABAergic neurons. *Dev Neurobiol* 2011; 71: 45–61.
16. Spatazza J, Lee HH, Di Nardo AA, et al. Choroid-plexus-derived Otx2 homeoprotein constrains adult cortical plasticity. *Cell Rep* 2013; 3: 1815–1823.
17. Cabungcal JH, Steullet P, Morishita H, et al. Perineuronal nets protect fast-spiking interneurons against oxidative stress. *Proc Natl Acad Sci USA* 2013; 110: 9130–9135.
18. Cardin JA, Carlen M, Meletis K, et al. Driving fast-spiking cells induces gamma rhythm and controls sensory responses. *Nature* 2009; 459: 663–667.
19. Sohal VS. Insights into cortical oscillations arising from optogenetic studies. *Biol Psychiatry* 2012; 71: 1039–1045.
20. Hashemi E, Ariza J, Rogers H, et al. The number of parvalbumin-expressing interneurons is decreased in the prefrontal cortex in autism. *Cereb Cortex* 2018; 28: 690.
21. Steullet P, Cabungcal JH, Coyle J, et al. Oxidative stress-driven parvalbumin interneuron impairment as a common mechanism in models of schizophrenia. *Mol Psychiatry* 2017; 22: 936–943.
22. Liu FF, Yang LD, Sun XR, et al. NOX2 mediated-parvalbumin interneuron loss might contribute to anxiety-like and enhanced fear learning behavior in a rat model of post-traumatic stress disorder. *Mol Neurobiol* 2016; 53: 6680–6689.
23. Xu X, Roby KD and Callaway EM. Immunochemical characterization of inhibitory mouse cortical neurons: three chemically distinct classes of inhibitory cells. *J Comp Neurol* 2010; 518: 389–404.
24. Lee JH, Durand R, Gradinaru V, et al. Global and local fMRI signals driven by neurons defined optogenetically by type and wiring. *Nature* 2010; 465: 788–792.
25. Wang H, Peca J, Matsuzaki M, et al. High-speed mapping of synaptic connectivity using photostimulation in

channelrhodopsin-2 transgenic mice. *Proc Natl Acad Sci USA* 2007; 104: 8143–8148.

26. Bauer AQ, Kraft AW, Baxter GA, et al. Effective connectivity measured using optogenetically evoked hemodynamic signals exhibits topography distinct from resting state functional connectivity in the mouse. *Cereb Cortex* 2018; 28: 370–386.

27. Wright PW, Brier LM, Bauer AQ, et al. Functional connectivity structure of cortical calcium dynamics in anesthetized and awake mice. *PLoS One* 2017; 12: e0185759.

28. Mattis J, Tye KM, Ferenczi EA, et al. Principles for applying optogenetic tools derived from direct comparative analysis of microbial opsins. *Nat Methods* 2011; 9: 159–172.

29. Bergonzi KM, Bauer AQ, Wright PW, et al. Mapping functional connectivity using cerebral blood flow in the mouse brain. *J Cereb Blood Flow Metab* 2015; 35: 367–370.

30. Boas DA and Dunn AK. Laser speckle contrast imaging in biomedical optics. *J Biomed Opt* 2010; 15: 011109.

31. White BR, Bauer AQ, Snyder AZ, et al. Imaging of functional connectivity in the mouse brain. *PLoS One* 2011; 6: e16322.

32. Bauer AQ, Kraft AW, Wright PW, et al. Optical imaging of disrupted functional connectivity following ischemic stroke in mice. *Neuroimage* 2014; 99: 388–401.

33. Jones M, Berwick J, Johnston D, et al. Concurrent optical imaging spectroscopy and laser-Doppler flowmetry: the relationship between blood flow, oxygenation, and volume in rodent barrel cortex. *Neuroimage* 2001; 13: 1002–1015.

34. Dunn AK, Devor A, Dale AM, et al. Spatial extent of oxygen metabolism and hemodynamic changes during functional activation of the rat somatosensory cortex. *Neuroimage* 2005; 27: 279–290.

35. Franceschini MA, Radhakrishnan H, Thakur K, et al. The effect of different anesthetics on neurovascular coupling. *NeuroImage* 2010; 51: 1367–1377.

36. Stefanovic B, Warnking JM and Pike GB. Hemodynamic and metabolic responses to neuronal inhibition. *Neuroimage* 2004; 22: 771–778.

37. Logothetis NK. The ins and outs of fMRI signals. *Nat Neurosci* 2007; 10: 1230–1232.

38. Ogawa S, Lee TM and Barrere B. The sensitivity of magnetic resonance image signals of a rat brain to changes in the cerebral venous blood oxygenation. *Magn Reson Med* 1993; 29: 205–210.

39. Lauritzen M, Mathiesen C, Schaefer K, et al. Neuronal inhibition and excitation, and the dichotomic control of brain hemodynamic and oxygen responses. *NeuroImage* 2012; 62: 1040–1050.

40. Markram H, Toledo-Rodriguez M, Wang Y, et al. Interneurons of the neocortical inhibitory system. *Nat Rev Neurosci* 2004; 5: 793–807.

41. Uhlirova H, Kilic K, Tian P, et al. The roadmap for estimation of cell-type-specific neuronal activity from non-invasive measurements. *Philos Trans R Soc Lond B Biol Sci* 2016; 371: 20150356.

42. Enager P, Piilgaard H, Offenhauser N, et al. Pathway-specific variations in neurovascular and neurometabolic coupling in rat primary somatosensory cortex. *J Cereb Blood Flow Metab* 2009; 29: 976–986.

43. Shmuel A, Augath M, Oeltermann A, et al. Negative functional MRI response correlates with decreases in neuronal activity in monkey visual area V1. *Nat Neurosci* 2006; 9: 569–577.

44. Shmuel A, Yacoub E, Pfeuffer J, et al. Sustained negative BOLD, blood flow and oxygen consumption response and its coupling to the positive response in the human brain. *Neuron* 2002; 36: 1195–1210.

45. Hillman EM. Coupling mechanism and significance of the BOLD signal: a status report. *Annu Rev Neurosci* 2014; 37: 161–181.

46. Hasenstaub A, Otte S, Callaway E, et al. Metabolic cost as a unifying principle governing neuronal biophysics. *Proc Natl Acad Sci* 2010; 107: 12329–12334.

47. Tremblay R, Lee S and Rudy B. GABAergic interneurons in the neocortex: from cellular properties to circuits. *Neuron* 2016; 91: 260–292.

48. Howard A, Tamas G and Soltesz I. Lighting the chandelier: new vistas for axo-axonic cells. *Trends Neurosci* 2005; 28: 310–316.

49. Zhu Y, Stornetta RL and Zhu JJ. Chandelier cells control excessive cortical excitation: characteristics of whisker-evoked synaptic responses of layer 2/3 nonpyramidal and pyramidal neurons. *J Neurosci* 2004; 24: 5101–5108.

50. Moraschi M, DiNuzzo M and Giove F. On the origin of sustained negative BOLD response. *J Neurophysiol* 2012; 108: 2339–2342.

51. Attwell D and Laughlin SB. An energy budget for signaling in the grey matter of the brain. *J Cereb Blood Flow Metab* 2001; 21: 1133–1145.

52. Erecinska M and Silver IA. ATP and brain function. *J Cereb Blood Flow Metab* 1989; 9: 2–19.

53. Kann O. The interneuron energy hypothesis: implications for brain disease. *Neurobiol Dis* 2016; 90: 75–85.

54. Packer AM and Yuste R. Dense, unspecific connectivity of neocortical parvalbumin-positive interneurons: a canonical microcircuit for inhibition? *J Neurosci* 2011; 31: 13260–13271.

55. Hu H, Gan J and Jonas P. Interneurons. Fast-spiking, parvalbumin(+) GABAergic interneurons: from cellular design to microcircuit function. *Science* 2014; 345: 1255263.

56. Rosenthal ZP, Raut RV, Yan P, et al. Local perturbations of cortical excitability propagate differentially through large-scale functional networks. *Cereb Cortex* 2020; 30: 3352–3369.

57. Galarreta M and Hestrin S. A network of fast-spiking cells in the neocortex connected by electrical synapses. *Nature* 1999; 402: 72–75.

58. Fukuda T and Kosaka T. Gap junctions linking the dendritic network of GABAergic interneurons in the hippocampus. *J Neurosci* 2000; 20: 1519–1528.

59. Packer AM, McConnell DJ, Fino E, et al. Axo-dendritic overlap and laminar projection can explain interneuron connectivity to pyramidal cells. *Cereb Cortex* 2012; 23: 2790–2802.

60. Ayling OG, Harrison TC, Boyd JD, et al. Automated light-based mapping of motor cortex by photoactivation of channelrhodopsin-2 transgenic mice. *Nat Methods* 2009; 6: 219–224.

61. Thomson AM and Lamy C. Functional maps of neocortical local circuitry. *Front Neurosci* 2007; 1: 19–42.

62. Vazquez AL, Fukuda M, Crowley JC, et al. Neural and hemodynamic responses elicited by forelimb- and photostimulation in channelrhodopsin-2 mice: insights into the hemodynamic point spread function. *Cereb Cortex* 2014; 24: 2908–2919.

63. Sheth SA, Nemoto M, Guiou MW, et al. Spatiotemporal evolution of functional hemodynamic changes and their relationship to neuronal activity. *J Cereb Blood Flow Metab* 2005; 25: 830–841.

64. Ramaswamy S and Markram H. Anatomy and physiology of the thick-tufted layer 5 pyramidal neuron. *Front Cell Neurosci.* Epub ahead of print 26 June 2015. DOI: 10.3389/fncel.2015.00233.

65. Almási Z, Dávid C, Witte M, et al. Distribution patterns of three molecularly defined classes of GABAergic neurons across columnar compartments in mouse barrel cortex. *Front Neuroanat* 2019; 13: 45.

66. Donahue MJ, Near J, Blicher JU, et al. Baseline GABA concentration and fMRI response. *NeuroImage* 2010; 53: 392–398.

67. Muthukumaraswamy SD, Edden RA, Jones DK, et al. Resting GABA concentration predicts peak gamma frequency and fMRI amplitude in response to visual stimulation in humans. *Proc Natl Acad Sci USA* 2009; 106: 8356–8361.

68. Tanahira C, Higo S, Watanabe K, et al. Parvalbumin neurons in the forebrain as revealed by parvalbumin-Cre transgenic mice. *Neurosci Res* 2009; 63: 213–223.

69. Desai M, Kahn I, Knoblich U, et al. Mapping brain networks in awake mice using combined optical neural control and fMRI. *J Neurophysiol* 2011; 105: 1393–1405.

70. Kahn I, Desai M, Knoblich U, et al. Characterization of the functional MRI response temporal linearity via optical control of neocortical pyramidal neurons. *J Neurosci* 2011; 31: 15086–15091.

71. Scott NA and Murphy TH. Hemodynamic responses evoked by neuronal stimulation via channelrhodopsin-2 can be independent of intracortical glutamatergic synaptic transmission. *PLoS One* 2012; 7: e29859.

72. Iordanova B, Vazquez AL, Poplawsky AJ, et al. Neural and hemodynamic responses to optogenetic and sensory stimulation in the rat somatosensory cortex. *J Cereb Blood Flow Metab* 2015; 35: 922–932.

73. Devor A, Tian P, Nishimura N, et al. Suppressed neuronal activity and concurrent arteriolar vasoconstriction may explain negative blood oxygenation level-dependent signal. *J Neurosci* 2007; 27: 4452–4459.

74. Lei H, Grinberg O, Nwaigwe CI, et al. The effects of ketamine-xylazine anesthesia on cerebral blood flow and oxygenation observed using nuclear magnetic resonance perfusion imaging and electron paramagnetic resonance oximetry. *Brain Res* 2001; 913: 174–179.

75. Masamoto K, Fukuda M, Vazquez A, et al. Dose-dependent effect of isoflurane on neurovascular coupling in rat cerebral cortex. *Eur J Neurosci* 2009; 30: 242–250.

76. Haseneder R, Kurz J, Dodt HU, et al. Isoflurane reduces glutamatergic transmission in neurons in the spinal cord superficial dorsal horn: evidence for a presynaptic site of an analgesic action. *Anesth Analg* 2004; 98: 1718–1723.

77. Sandstrom DJ. Isoflurane depresses glutamate release by reducing neuronal excitability at the Drosophila neuromuscular junction. *J Physiol* 2004; 558: 489–502.

78. Wu XS, Sun JY, Evers AS, et al. Isoflurane inhibits transmitter release and the presynaptic action potential. *Anesthesiology* 2004; 100: 663–670.

79. Ranft A, Kurz J, Deuringer M, et al. Isoflurane modulates glutamatergic and GABAergic neurotransmission in the amygdala. *Eur J Neurosci* 2004; 20: 1276–1280.

80. Hentschke H, Schwarz C and Antkowiak B. Neocortex is the major target of sedative concentrations of volatile anaesthetics: strong depression of firing rates and increase of GABA$_A$ receptor-mediated inhibition. *Eur J Neurosci* 2005; 21: 93–102.

81. Dickinson R, Peterson BK, Banks P, et al. Competitive inhibition at the glycine site of the N-methyl-D-aspartate receptor by the anesthetics xenon and isoflurane: evidence from molecular modeling and electrophysiology. *Anesthesiology* 2007; 107: 756–767.

82. Kelly EW, Solt K and Raines DE. Volatile aromatic anesthetics variably impact human gamma-aminobutyric acid type A receptor function. *Anesth Analg* 2007; 105: 1287–1292.

83. Eger EI II. The pharmacology of isoflurane. *Br J Anaesth* 1984; 56 (Suppl 1): 71S–99S.

84. Iida H, Ohata H, Iida M, et al. Isoflurane and sevoflurane induce vasodilation of cerebral vessels via ATP-sensitive K+ channel activation. *Anesthesiology* 1998; 89: 954–960.

85. Buxton RB, Uludag K, Dubowitz DJ, et al. Modeling the hemodynamic response to brain activation. *NeuroImage* 2004; 23 (Suppl 1): S220–S233.

86. Ances BM, Wilson DF, Greenberg JH, et al. Dynamic changes in cerebral blood flow, O$_2$ tension, and calculated cerebral metabolic rate of O$_2$ during functional activation using oxygen phosphorescence quenching. *J Cereb Blood Flow Metab* 2001; 21: 511–516.

87. Baron JC. Perfusion thresholds in human cerebral ischemia: historical perspective and therapeutic implications. *Cerebrovasc Dis* 2001; 11 (Suppl 1): 2–8.

88. Devor A, Hillman EM, Tian P, et al. Stimulus-induced changes in blood flow and 2-deoxyglucose uptake dissociate in ipsilateral somatosensory cortex. *J Neurosci* 2008; 28: 14347–14357.

89. Lim DH, Mohajerani MH, Ledue J, et al. In vivo large-scale cortical mapping using channelrhodopsin-2 stimulation in transgenic mice reveals asymmetric and reciprocal relationships between cortical areas. *Front Neural Circuit* 2012; 6: 11.

90. Rock C, Zurita H, Lebby S, et al. Cortical circuits of callosal GABAergic neurons. *Cereb Cortex* 2018; 28: 1154–1167.